Chinese Chemical Letters 36 (2025) 109897

Contents lists available at ScienceDirect

Chinese Chemical Letters

journal homepage: www.elsevier.com/locate/cclet

Reduced graphene oxide assembled on the Si nanowire anode enabling low passivation and hydrogen evolution for long-life aqueous Si-air batteries

Fengjun Deng[1], Tingyu Zhao[1], Xiaochen Zhang, Kaiyong Feng, Ze Liu, Youlin Xiang, Yingjian Yu*

College of Physics Science and Technology, Kunming University, Kunming 650214, China

ARTICLE INFO

Article history:
Received 15 January 2024
Revised 12 February 2024
Accepted 16 April 2024
Available online 16 April 2024

Keywords:
Si-air batteries
Reduced graphene oxide
Si NWs
Passivation
Corrosion

ABSTRACT

Silicon-air batteries (SABs), a new type of semiconductor air battery, have a high energy density. However, some side reactions in SABs cause Si anodes to be covered by a passivation layer to prevent continuous discharge, and the anode utilization rate is low. In this work, reduced graphene oxide (RGO) fabricated *via* high-temperature annealing or L-ascorbic acid (L.AA) reduction was first used to obtain Si nanowires/RGO-1000 (Si NWs/RGO-1000) and Si nanowires/RGO-L.AA (Si NWs/RGO-L.AA) composite anodes for SABs. It was found that RGO suppressed the passivation and self-corrosion reactions and that SABs using Si NWs/RGO-L.AA as the anode can discharge for more than 700 h, breaking the previous performance of SABs, and that the specific capacity was increased by 90.8% compared to bare Si. This work provides a new solution for the design of high specific capacity SABs with nanostructures and anode protective layers.

As the demand for energy increases, people need to research high-energy-density battery systems [1]. Metal-air batteries have attracted the attention of scientists because of their high theoretical energy density and cost-effectiveness [2–10]. A metal-air battery mainly consists of a metal anode, an electrolyte, a separator, and an air cathode [11]. When it works, the anode mainly releases electrons through the external circuit, and the cathode mainly participates in the reaction with oxygen in the air. Lithium-air batteries, zinc-air batteries, aluminum-air batteries, magnesium-air batteries, iron-air batteries, *etc*., which are currently widely studied, all face some unresolved problems, such as the formation of dendrites causing battery short circuits, poor stability, and short lifespan [12–17]. In addition to metals, semiconductor materials such as Si and Ge are currently also used as anode materials for air batteries [18–21]. Since Ein-Eli *et al.* proposed silicon-air batteries (SABs) in 2009 [22], SABs have been continuously explored [23,24]. SABs have a slightly higher specific energy density (5360 Wh/kg) than lithium-air batteries (5200 Wh/kg) [25]. Compared to metals such as lithium and zinc, silicon is abundant and easily accessible in the earth's crust. The main product of SABs reaction is SiO_2. The post-processing of SiO_2 does not cause any environmental pollution. Currently, two main types of electrolytes are used in SABs. One is EMI·2.3 HF·F ionic liquid-based electrolyte [26–28], but this electrolyte can cause serious chemical safety problems when used. The other is alkaline electrolyte [29–32], which does not harm the environment. The main reactions of the SABs during operation with alkaline electrolyte are as follows (Reactions 1–4):

$$\text{Cathode: } O_2 + 2H_2O + 4e^- \rightarrow 4OH^- \quad (1)$$

$$\text{Anode: } Si + 4OH^- \rightarrow Si(OH)_4 + 4e^- \quad (2)$$

$$\text{Formation of passivation layer: } Si(OH)_4 \rightarrow SiO_2 + 2H_2O \quad (3)$$

$$\text{Self-corrosion: } Si + 2OH^- + 2H_2O \rightarrow SiO_2(OH)_2{}^{2-} + 2H_2 \quad (4)$$

Reaction 3 reveals that the formation of the passivation layer interrupts the continuous discharge of the battery. Reaction 4 indicates that self-corrosion occurs during battery operation, resulting in significant ineffective consumption of silicon and a decrease in the specific capacity of the battery. Therefore, it is urgent to further

* Corresponding author.
E-mail address: yuyingjiankmu@163.com (Y. Yu).
[1] These authors contributed equally to this work.

https://doi.org/10.1016/j.cclet.2024.109897
1001-8417/

ameliorate the anode materials of SABs and increase the anode utilization rate of the battery.

Etching the anode to form nanowires (NWs) is an effective anti-passivation method for SABs. Zhong *et al*. used Si with etched NWs as the anode of SABs, which could discharge continuously, while the unetched Si anode could only discharge for less than 10 min [29]. Chen *et al*. studied the discharge threshold of P(100) and N(100) Si with etched NWs as anodes of SABs [23]. This study showed that at the current density of 0.03 mA/cm^2, 1.9 mol/L KOH was the lowest threshold for P-type Si, and N-type Si can discharge for more than 500 h at 0.05 mA/cm^2 in 6 mol/L KOH. The reason why Si NWs can improve battery performance is that the specific surface area of Si anode increases significantly after etching. This also leads to an accelerated dissolution rate of $Si(OH)_4$, which reduces the accumulation of SiO_2 on the Si surface and allows SABs to discharge. Although nanostructured Si anode can improve the performance of SABs, the self-corrosion still causes Si waste. Therefore, fabrication of a protective layer on nanostructured Si is a promising method to inhibit self-corrosion and improve the performance of SABs.

Due to their good chemical stability and strong tunability, many methods of applying protective carbonaceous materials to optimize electrodes have been reported, such as metal organic framework, covalent organic framework, and graphene materials [33–38]. Since Novoselov and co-workers isolated a single-atom carbon layer in 2004, graphene materials have attracted the interest of scientific researchers due to their high conductivity and excellent physico-chemical properties [39]. In recent years, there have been some reports on the application of graphene materials to enhance the performance of anode materials in metal or semiconductor-based batteries. For example, Zhao *et al*. successfully fabricated a Ge/graphene composite electrode for Ge-air batteries [20]. The protective graphene layer effectively inhibited the passivation reaction, induced the flat deposition of the passivation layer, and reduced chemical corrosion and hydrogen evolution reaction, thereby achieving a breakthrough in long-term stability. Compared to bare Ge anodes without a graphene protective layer, the discharge time of the battery assembled with Ge/graphene anode was extended by 38.9%–90.3%, and the power density was higher. Dong *et al*. demonstrated an extended and exceptional cycling stability of up to 170 days in the Zn//Zn battery using the improved RGO@ZnSi [40]. RGO@ZnSi possessed a zinc ion transport channel and exhibited an affinity for zinc. Meanwhile, the introduction of reduced graphene oxide (RGO) significantly enhanced its conductivity. Currently, the method of obtaining RGO through electrochemical reduction of graphene oxide (GO) is considered a suitable method for low-cost and large-scale production [41]. Lockett *et al*. utilized multilayer graphene oxide and silicon nanowires to prepare CVD-rMGO/Si NWs composite materials *via* chemical vapor deposition (CVD). This composite material, serving as a binder-free anode for lithium-ion batteries, achieved a specific capacity of 2247 mAh/g, with a capacity retention of 842 mAh/g after 90 cycles. This achievement is primarily attributed to the conversion of highly ordered multilayer graphene produced by CVD into reduced multilayer graphene oxide (CVD-rMGO), which enhances internal adhesion, maintains reduced thickness, and concurrently exhibits high capacity and cycling ability. The CVD-rMGO film features numerous pores, aiding in preventing anisotropic lithiation and delithiation, and also possesses the capability to support intercalation of highly active materials [42].

Due to the excellent electrochemical performance of RGO, in this work, we reduced GO to RGO by high-temperature annealing or by reaction with L-ascorbic acid (L.AA), and Si nanowires/RGO-1000 (Si NWs/RGO-1000) and Si nanowires/RGO-L.AA (Si NWs/RGO-L.AA) composite materials were successfully prepared. The crystallization degree of RGO under different reaction conditions was explored. Afterwards, the composite anode, 6 mol/L KOH electrolyte, and Pt/C cathode were assembled into an alkaline aqueous SABs for electrochemical testing. Using bare Si and Si NWs anodes as comparative references, the effects of the two Si NWs/RGO anodes on the performance of SABs were investigated. The results showed that RGO had a significant effect on improving the performance of SABs.

In this work, two different methods were used to prepare Si NW/RGO composite anodes, as shown in Fig. 1. The materials, fabrication and characterization methods are illustrated in Supporting Information. To prove the successful conversion of GO to RGO, we conducted XRD, Raman, XPS, and HRTEM characterization. It can be seen from Fig. S1a (Supporting information) that GO has a sharp diffraction peak at $2\theta = 10.3°$. The peak position of natural graphite should be at $2\theta = 26.6°$. After oxidation, its peak position changes from $2\theta = 26.6°$ to $2\theta = 10.3°$. This is attributed to the oxygen-containing functional groups (-OH, -COOH, *etc*.) inserted between the lamellae of the oxidized graphite, which increases interlayer spacing. After high-temperature annealing or reduction by L.AA, the (001) peak of GO disappeared, and the broad peak (002) appeared in the two reduced materials. This is mainly due to the removal of oxygen-containing functional groups during the reduction process. Fig. S1b (Supporting information) shows the Raman spectra of GO, RGO-1000, and RGO-L.AA. G-band for GO, RGO-1000, and RGO-L.AA appears at 1594, 1597, and 1599 cm^{-1}, respectively, and the peaks are blue-shifted to high frequencies. The values of I_D/I_G are 0.99, 1.01, and 1.02, respectively, indicating that the degree of defects in the RGO becomes larger. The C 1s fine spectrum of XPS is used to characterize the chemical state before and after reduction. As shown in Figs. S1c–e (Supporting information), the C–O–C and O–C=O functional groups of RGO-1000 and RGO-L.AA are significantly reduced, which is further evidence that GO is reduced. The TEM characterization of RGO-1000 and RGO-L.AA is shown in Fig. 2. HRTEM images of RGO-1000 and RGO-L.AA are shown in Figs. 2a and d, respectively. The lattice stripes of the two RGOs can be clearly seen in the pictures. The diffraction ring images of RGO-1000 and RGO-L.AA (Figs. 2b and e) clearly show that the crystallinity of RGO-L.AA is higher than that of RGO-1000.

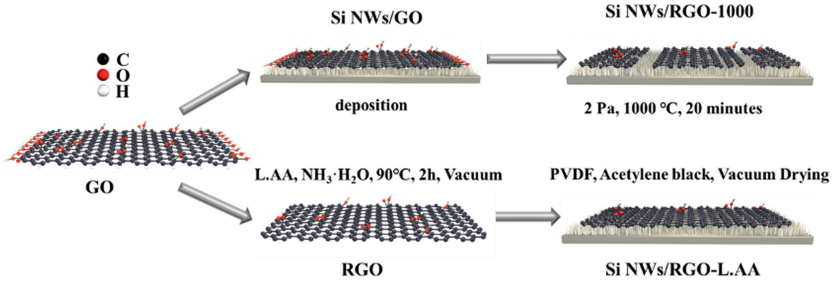

Fig. 1. Two different methods to prepare Si NW/RGO composite anodes.

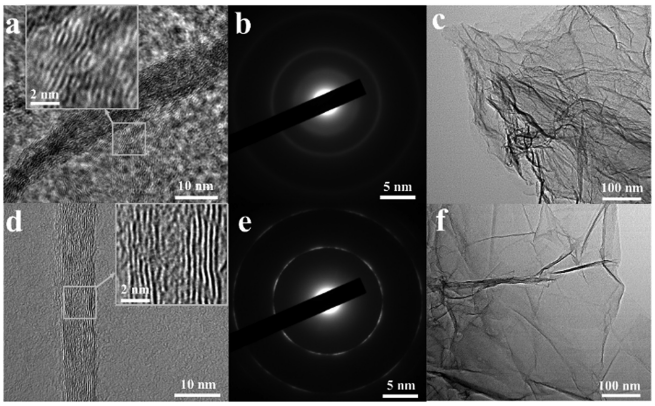

Fig. 2. (a) HRTEM images of RGO-1000. (b) Diffraction ring of RGO-1000. (c) TEM images of RGO-1000. (d) HRTEM images of RGO-L.AA. (e) Diffraction ring of RGO-L.AA. (f) TEM images of RGO-L.AA.

Figs. 2c and f are TEM images of RGO-1000 and RGO-L.AA, respectively, in which the layered structure and darker wrinkles of RGO can also be clearly seen.

To demonstrate the composite situation of RGO and Si NWs, the surface of composite samples was examined under different conditions with the SEM. Planar bare Si presents a smooth surface structure (Fig. 3a), and the porous structure of Si NWs provides active sites for RGO compound (Fig. 3b). When Si NWs were deposited in the GO dispersion for one hour, the GO layer on the Si NWs could be clearly observed (Fig. 3c). Fig. 3d provides a cross-sectional SEM of Si NWs/GO. It can be clearly observed that GO was deposited thickly on the NWs. After high-temperature treatment, the amount of GO decreases due to internal reactions and is more tightly bound to the substrate (Fig. 3e). Fig. 3f shows the cross-sectional view of Si NWs/RGO-1000. Compared to the sample before high-temperature treatment, the RGO layer of Si NWs/RGO-1000 after treatment is thinner and only some flocs can be seen. The SEM image of the surface of Si NWs/RGO-L.AA composite anode is shown in Fig. 3g. The large-area combination of RGO-L.AA and Si NWs can be clearly observed. The cross-sectional SEM image (Fig. 3h) and the large-scale surface SEM image (Fig. S2 in Supporting information) of Si NWs/RGO-L.AA also demonstrate the uniform deposition of RGO on Si NWs. Table S1 (Supporting information) shows the elemental composition of different materials during processing. After the Si wafer has been cleaned, the oxygen content on the surface is extremely low, indicating effective cleaning of Si wafer. When the Si wafer is etched and the nanowire structure is formed on the Si surface, the porous surface accelerates Si oxidation and the oxygen content increases. The carbon contents of the Si NWs/RGO-1000 and Si NWs/RGO-L.AA composites increase to 15.56% and 54.81%, which proves the successful compounding of RGO on Si NWs. To further verify the interaction between water and anode materials, we tested the surface water contact angle (CA) of four anode materials (Fig. S3 in Supporting information). The CA of bare Si is 30.62°. After the Si wafer is etched, the CA of Si NWs becomes 19.93°, and its hydrophilicity becomes stronger. The CA of Si NWs/RGO-1000 and Si NWs/RGO-L.AA is 47.59° and 52.83°, respectively, which is larger than those of bare Si and Si NWs. This suggests that RGO in the composite anode can reduce the contact between water and Si, which helps to inhibit the self-corrosion and extend the life of the battery.

To explore the advantages of RGO-coated Si as anode for SABs, we tested the electrochemical and full-cell performance of Si NWs/RGO under different conditions. Simultaneously, we conducted tests on bare Si and Si NWs anodes for comparison. To investigate the difference in anode corrosion, we measured the dynamic polarization curves of SABs of bare Si, Si NWs, Si NWs/RGO-1000, and Si NWs/RGO-L.AA (Fig. 4a). The corrosion potential of Si NWs/RGO-L.AA (1.46 V) is the highest, while that of bare Si (1.27 V) is the lowest. The corrosion current densities of different anodes are shown in Table S2 (Supporting information), where the corrosion current of Si NWs is the highest (1.38×10^{-4} mA/cm^2). This may be attributed to the fact that the specific surface area of the Si wafer increases after etching, which leads to more active sites for the corrosion reaction. Compared with other three anodes, Si NWs/RGO-L.AA shows the lowest corrosion current (1.016×10^{-5} mA/cm^2), revealing that the Si surface composed by RGO-L.AA is more corrosion-resistant. Fig. 4b displays the electrochemical impedance spectroscopy (EIS) of four anodes. It is evident that the charge transfer resistance of the two anode materials compounded with RGO is lower than that of bare Si and Si NWs, which proves that RGO favors charge transfer during the discharge process. Fig. 4c shows the actual current-potential (*J*-*V*) and power-density curves of SABs with various anodes. It can be observed that the battery voltage of the four different anodes decreases with increasing current density and the three processed anodes exhibit a significant increase in maximum discharge current compared to bare Si. The maximum power density of bare silicon is 0.0063 mW/cm^2; after the formation of Si NWs structure, the maximum power density increases to 0.0639 mW/cm^2. In the SAB with a Si NWs/RGO-1000 anode, the maximum power density of 0.0173 mW/cm^2 is slightly lower compared to Si NWs, attributed to the higher interfacial resistance at the surface after annealing. The SAB using a Si NWs/RGO-L.AA anode exhibits the best performance in terms of both maximum power density (0.3512 mW/cm^2) and maximum discharge current density (0.9258 mA/cm^2), surpassing the previous work [24]. Moreover, at a voltage of 0.6 V, Si NWs/RGO-L.AA demonstrates a significantly higher maximum current density of 0.5717 mA/cm^2 than in Ref. [24]. This may be due to the ideal conductivity of the L.AA-treated RGO interlayer. To investigate the voltage of SABs under different current densities,

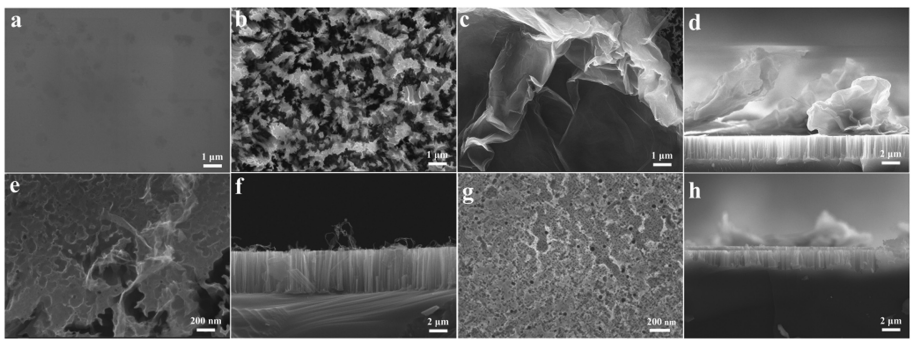

Fig. 3. Top-view SEM images of (a) bare Si, (b) Si NWs, (c) Si NWs/GO, (e) Si NWs/RGO-1000, and (g) Si NWs/RGO-L.AA; Cross-sectional SEM images of (d) Si NWs/GO, (f) Si NWs/RGO-1000, and (h) Si NWs/RGO-L.AA.

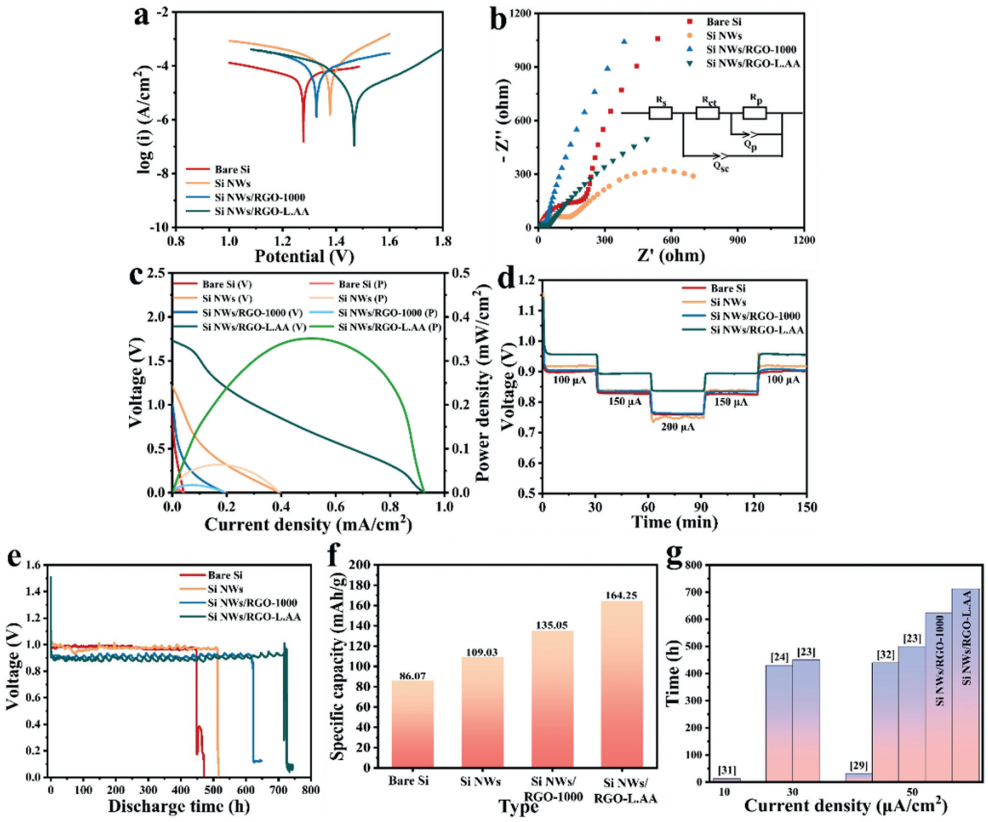

Fig. 4. (a) Tafel curves, (b) EIS, (c) *J-V* and power density curves, (d) bare Si, Si NWs, Si NWs/RGO-1000, and Si NWs/RGO-L.AA anodes discharging at 100, 150, and 200 μA for 30 min each. (e) Constant current discharge characteristics at 150 μA, (f) specific capacity for Si-air batteries assembled with bare Si, Si NWs, Si NWs/RGO-1000, and Si NWs/RGO-L.AA as anodes, respectively. (g) Comparison with discharge duration in other studies.

we conducted a 150-min step discharge test, as shown in Fig. 4d. The current started from 100 μA and increased by 50 μA at 30-min intervals until it reached 200 μA and then returned to 100 μA. As the current increases, the discharge voltage decreases. The voltage of Si NWs/RGO-1000 fluctuates during the process, but that of Si NWs/RGO-L.AA is stable throughout the process. Finally, we performed constant current discharge tests on bare Si, Si NWs, Si NWs/RGO-1000, and Si NWs/RGO-L.AA anode assembled cells at a current of 150 μA (Fig. 4e). Compared to bare Si, Si NWs reduce the accumulation of the passivation layer during the discharge process due to the increase in specific surface area [23], thereby extending the discharge time. Composited by RGO, Si NWs/RGO-1000 anode extends the discharge time to more than 600 h, and Si NWs/RGO-L.AA anode can even extend the discharge time to more than 700 h. This extension is primarily due to the increased specific surface area of the composite anode and the inhibitory effect of the presence of the RGO layer on the self-corrosion and passivation reaction. The thickness of RGO in Si NWs/RGO-L.AA is thicker than that in Si NWs/RGO-1000. It is reasonable that a relatively thicker RGO layer may provide greater assistance in restraining corrosion and passivation, thus enhancing the battery performance. The specific capacities of SABs with the four types of anodes are shown in Fig. 4f. Compared with bare Si, the specific capacities of Si NWs/RGO-1000 and Si NWs/RGO-L.AA increase by 50% and 90.8%, respectively. Compared with the specific capacity of MOS-modified SABs studied by Chen *et al.* (114 mAh/g) [24], Si NWs/RGO-1000 (135.05 mAh/g) and Si NWs/RGO-L.AA (164.25 mAh/g) anode show a significant improvement. We summarized the discharge durations of SABs at current densities of 10, 30, and 50 μA/cm^2, using KOH as the electrolyte (Fig. 4g). From the results, it is evident that the SABs with Si NWs/RGO-L.AA have the longest discharge duration in this work.

To delve into the impact of two Si/RGO composite anodes on SABs, we explored changes in anode surface morphology after discharge. SEM images (Figs. S4a–d in Supporting information) depict the surface morphology of the four anode materials after discharging at 150 μA for 20 h. Apparently, the bare Si anode exhibits a relatively smooth surface with more electrolyte gel containing silicate and silica. This is due to the passivation of the anode during discharge, leading to water consumption in the electrolyte and an increase in by-products. During prolonged discharge, the electrolyte transforms from a liquid to a gel and these by-products continue to adsorb on the Si surface. When bare Si is processed into Si NWs, Si NWs/RGO-1000, and Si NWs/RGO-L.AA structures, the anode surface exhibits a convex block structure after discharge. This indicates that the adsorption of by-products on the modified anode surface becomes weaker. The Si NWs/RGO-L.AA composite anode has fewer surface irregularities, and the EDS image (Fig. S5 in Supporting information) reveals a relatively uniform distribution of carbon and oxygen elements on the surface. To further verify the passivation degree of the anode surfaces during discharge, the cross-sectional morphology (Figs. S4e–h in Supporting information) of different anodes was characterized after discharging for 20 h at 150 μA. The passivation layer thicknesses of bare Si, Si NWs, Si NWs/RGO-1000, and Si NWs/RGO-L.AA are about 47, 33, 24, and 19 μm, respectively. Compared to bare Si, the passivation layer on Si NWs, Si NWs/RGO-1000, and Si NWs/RGO-L.AA anodes after discharge appears thinner, indicating effective passivation inhibition by RGO coating. To further validate this conclusion, SEM images of the four anodes were tested under constant current discharge at 150 μA for 40 h and 60 h (Figs. S6 and S7 in Supporting information). After 40 h and 60 h of discharge, the surface of the bare Si anode gradually appears in a long strip shape, and the block structure on the surface of the other three anodes slowly becomes

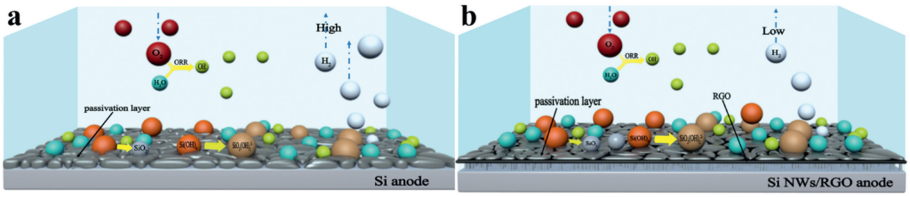

Fig. 5. Diagram of discharge mechanisms of (a) bare Si and (b) Si NWs/RGO as anodes in Si-air batteries.

larger. However, Si NWs/RGO-L.AA maintains the smallest block shape. From the above results, it is evident that as discharge time increases, the passivation layer on the surface of the four negative electrode materials gradually thickens. However, Si NWs/RGO-L.AA exhibits the strongest anti-passivation effect. Oxygen content on the surface of the four anode materials after different discharge times is shown in Table S3 (Supporting information). The oxygen content on the surface of Si NWs/RGO-L.AA is consistently the lowest over different time periods, further proving RGO-L.AA's superior protective effect on the battery anode.

To further illustrate the significant effect of the RGO protective layer during discharge process, the discharge mechanism diagram is shown in Fig. 5. In the initial discharge process, the Si anode is transformed to Si hydroxide into the electrolyte. Part of Si hydroxide dehydrates and forms a SiO_2 passivation layer on the Si surface. Part of this layer is also dissolved to a certain extent by the electrolyte to achieve dynamic equilibrium. The presence of the RGO layer reduces the affinity of the anode surface to water, resulting in less contact between Si and water, which plays a positive role in inhibiting self-corrosion. The results observed through *in-situ* optical microscopy (Fig. S8 in Supporting information) indicate that, in KOH, Si NWs exhibit significant bubble formation, whereas no significant bubbles are observed for Si NWs/RGO-1000 and Si NWs/RGO-L.AA. This further confirms the effective inhibition of the self-corrosion reaction by the RGO layer. Furthermore, the modified anode exhibits reduced adsorption capacity for by-products, leading to a decrease in the passivation layer on the anode surface. The RGO layer protects the Si anode and improves the actual discharge capacity of the SABs.

In this study, we successfully utilized high-temperature annealing and L.AA to reduce GO for the first time and prepared two composite anodes for SABs, Si NWs/RGO-1000, and Si NWs/RGO-L.AA. We investigated the influence of the RGO protective layer on the discharge characteristics of aqueous alkaline SABs. The research results show that Si NWs/RGO-L.AA exhibit outstanding conductivity, robust resistance to self-corrosion and passivation reactions. Consequently, in the constant current discharge test at 150 μA, SABs using the Si NWs/RGO-L.AA as the anode can discharge for more than 700 h and exhibit the highest power density. In conclusion, the use of RGO as a protective layer for SABs is practical to reduce silicon waste and improve the specific capacity of the battery.

Declaration of competing interest

The authors declare that they have no known competing financial interests or personal relationships that could have appeared to influence the work reported in this paper.

Acknowledgments

This work was financially supported by the National Natural Science Foundation of China (No. 61904073), Spring City Plan-Special Program for Young Talents (No. K202005007), Yunnan Talents Support Plan for Yong Talents (No. XDYC-QNRC-2022-0482), Yunnan Local Colleges Applied Basic Research Projects (No. 202101BA070001-138), Scientific Research Fund of Yunnan Education Department (No. 2023Y0883), Frontier Research Team of Kunming University 2023, and Key Laboratory of Artificial Microstructures in Yunnan Higher Education.

Supplementary materials

Supplementary material associated with this article can be found, in the online version, at doi:10.1016/j.cclet.2024.109897.

References

[1] S. Zaidi, X. Li, Adv. Energy Mater. 13 (2023) 2300985.
[2] G. Dias, J. Costa, A. Neto, Adv. Colloid Interface Sci. 315 (2023) 102891.
[3] Y. Chen, J. Xu, P. He, et al., Sci. Bull. 67 (2022) 2449–2486.
[4] D. Zhong, K. Wang, Y. Zuo, et al., J. Mater. Chem. A 11 (2023) 25115–25135.
[5] X. Lv, Z. Wang, Z. Lai, et al., Small 20 (2024) 2306396.
[6] A. Sinha, T. Thomas, D. Mandal, Energy Stor. Mater. 63 (2023) 102988.
[7] M. Wei, K. Wang, Y. Zuo, et al., Adv. Funct. Mater. 33 (2023) 2302243.
[8] W. Liang, F. Lian, N. Meng, et al., Energy Stor. Mater. 28 (2020) 350–356.
[9] M. Liu, Q. Zhang, X. Zhang, et al., Chem. Eng. J. 472 (2023) 145154.
[10] Y. Qiu, G. Li, H. Zhou, et al., Adv. Sci. 10 (2023) 2300482.
[11] H. Zhou, L. Guo, R. Zhang, et al., Adv. Funct. Mater. 33 (2023) 2304154.
[12] Y. Sun, X. Liu, Y. Jiang, et al., J. Mater. Chem. A 7 (2019) 18183–18208.
[13] F. Tong, S. Wei, X. Chen, W. Gao, J. Magnes. Alloy. 9 (2021) 1861–1883.
[14] J. Chen, J. Luo, Y. Xiang, Y. Yu, J. Energy Chem. 91 (2024) 178–193.
[15] Q. Wang, L. Ren, T. Lu, et al., ACS Energy Lett. 8 (2023) 4441–4464.
[16] X. Zhong, Y. Shao, B. Chen, et al., Adv. Mater. 35 (2023) 2301952.
[17] Q. Wang, S. Kaushik, X. Xiao, Q. Xu, Chem. Soc. Rev. 52 (2023) 6139–6190.
[18] Y. Yu, S. Hu, Chin. Chem. Lett. 32 (2021) 3277–3287.
[19] A. Inoishi, T. Sakai, Y. Ju, S. Ida, T. Ishihara, J. Mater. Chem. A 1 (2013) 15212–15215.
[20] T. Zhao, Y. Zhang, D. Wang, et al., Carbon 205 (2023) 86–96.
[21] Y. Zhang, S. Gao, T. Zhao, et al., Arab. J. Chem. 16 (2023) 105021.
[22] G. Cohn, D. Starosvetsky, R. Hagiwara, D. Macdonald, Y. Ein-Eli, Electrochem. Commun. 11 (2009) 1916–1918.
[23] D. Chen, Y. Li, X. Zhang, S. Hu, Y. Yu, J. Ind. Eng. Chem. 112 (2022) 271–278.
[24] D. Chen, X. Zhang, Y. Zhang, et al., Surf. Interfaces 38 (2023) 102777.
[25] R. Bansal, P. Menon, R. Sharma, SN Appl. Sci. 2 (2020) 1141.
[26] G. Cohn, D. Macdonald, Y. Ein-Eli, ChemSusChem 4 (2011) 1124–1129.
[27] Y. Durmus, C. Roitzheim, H. Tempel, et al., J. Appl. Electrochem. 50 (2019) 93–109.
[28] P. Jakes, G. Cohn, Y. Ein-Eli, et al., ChemSusChem 5 (2012) 2278–2285.
[29] X. Zhong, H. Zhang, Y. Liu, et al., ChemSusChem 5 (2012) 177–180.
[30] R. Schalinski, S. Schweizer, R. Wehrspohn, ChemSusChem 16 (2023) e20230077.
[31] D. Park, S. Kim, J. Ocon, et al., ACS Appl. Mater. Interfaces 7 (2015) 3126–3132.
[32] R. Schalinski, P. Mörstedt, S. Schweizer, R. Wehrspohn, Adv. Energ. Sust. Res. 4 (2023) 2300138.
[33] F. Deng, Y. Zhang, Y. Yu, Batteries 9 (2023) 109.
[34] K. Feng, D. Wang, Y. Yu, Molecules 28 (2023) 2721.
[35] Y. Zhao, K. Feng, Y. Yu, Adv. Sci. 11 (2024) 2308087.
[36] Y. Zhao, C. Yang, Y. Yu, Chin. Chem. Lett. 35 (2024) 108865.
[37] W. Liu, D. Rao, J. Bao, et al., J. Energy Chem. 57 (2021) 428–435.
[38] Z. Liu, X. Zhang, J. Luo, Y. Yu, Chin. Chem. Lett. 35 (2024) 109500.
[39] R. Raccichini, A. Varzi, S. Passerini, B. Scrosati, Nat. Mater. 14 (2014) 271–279.
[40] X. Dong, Y. Peng, Y. Wang, et al., Energy Stor. Mater. 62 (2023) 102937.
[41] M. Fathy, A. Gomaa, F. Taher, M. El-Fass, J. Mater. Sci. 51 (2016) 5664–5675.
[42] M. Lockett, V. Sarmiento, M. Gonzalez, et al., ACS Appl. Energy Mater. 4 (2021) 6391–6398.